FERMILAB-PUB-24-0768-PPD

Prepared for submission to JCAP

Study of the muon component in the core-corona model using CONEX 3D

Ana Martina Botti[a], **Isabel Astrid Goos**[b,*], **Matias Perlin**[c], **and Tanguy Pierog**[c]

[a]Fermi National Accelerator Laboratory (Fermilab)
PO Box 500, Batavia IL, 60510, USA
[b]Laboratoire Astroparticule et Cosmologie (APC)
10 Rue Alice Domon et Léonie Duquet, 75013 Paris, France
[c]Karlsruher Institut für Technologie (KIT), Institute for Astroparticle Physics,
Hermann-von-Helmholtz-Platz 1, 76344 Eggenstein-Leopoldshafen, Germany

E-mail: goos@apc.in2p3.fr

Abstract. The discrepancy between models and data on the muon content in air showers generated by ultra-high energy cosmic rays still needs to be solved. The CONEX simulation framework provides a flexible tool to assess the impact of different interaction properties and address the muon puzzle. In this work, we present the multidimensional extension of CONEX and show its performance compared to CORSIKA by discussing muon-related air-shower features for three experiments: KASCADE, IceTop, and the Pierre Auger Observatory. We also implement an effective version of the core-corona model to demonstrate the impact of the core effect, as observed at the LHC, on the muon content in air showers produced by ultra-high energy cosmic rays. At a primary energy of $E_0 = 10^{19}$ eV, we obtain an increase of 15% to 20% in the muon content.

Keywords: ultra high energy cosmic rays, cosmic ray experiments, cosmic ray theory

*Corresponding author

Contents

1 The muon puzzle

Several riddles remain open in the fields of high and ultra-high energy cosmic rays. For energies above 10^{15} eV, we can only detect cosmic rays indirectly through the secondary particles, or extensive air showers, produced when they interact with nuclei in the Earth's atmosphere [1]. The Heitler-Matthews model [2] describes the particle production in air showers in a simplified way: neutral pions, created along the shower, decay to photons that feed the electromagnetic component (encompassing photons, electrons, and positrons) by subsequent pair creation and Bremsstrahlung processes. Alongside neutral pions, charged pions typically decay into muons, forming the muonic component.

This model reveals two mass- and energy-sensitive observables [3]: the atmospheric depth at the maximum development of the cascade, $X_{\max}$, mainly determined by the electromagnetic component of the shower, and the number of muons at ground level, N_μ, driven by the shower's hadronic core. Then, we use simulations to interpret air shower measurements and to deduce, for example, the mean logarithmic mass of cosmic rays $\langle \ln A \rangle$ from $X_{\max}$ and N_μ. Most of the uncertainty in $\langle \ln A \rangle$ stems from the discrepancies in these models. This uncertainty ultimately challenges our understanding of the astrophysical scenarios in which cosmic rays are produced and accelerated.

Currently, the discrepancy between the muon density measured with surface arrays and that predicted by hadronic interaction models [4] represents one of the most significant questions in air shower physics. Refs. [4, 5] report on the so-called *muon puzzle*, observed in a broad energy range from about 10^{16} eV up to 10^{20} eV, and in experiments measuring showers under different atmospheric conditions with diverse detection techniques. In addition, the number of muons is also sensitive to hadronic multiparticle production at lower energies [6], which further expands the energy range that we need to revise in the models.

Air-shower experiments located at different altitudes measure the shower development at different stages, challenging the data interpretation. Following [4, 5], we categorized the experiments into three groups: the IceCube Neutrino Observatory with its surface array IceTop at around 2800 m a.s.l., the Pierre Auger Observatory and the HiRes/MIA Experiment

at ca. 1500 m a.s.l., all other experiments are located between 100 - 250 m a.s.l.. To compare simulations associated with different conditions, we discuss the cases of IceTop at IceCube, the Pierre Auger Observatory, and the KASCADE Experiment [7–9]. These cover different altitudes, energy ranges, distances to the shower core, and experimental configurations.

The Pierre Auger Observatory is a hybrid detector comprising a 3000 km^2 surface array of over 1600 water Cherenkov detectors and 24 fluorescence telescopes overlooking the layout from the periphery [7, 10]. It is located close to Malargüe, in Argentina, at an average altitude of ~ 1400 m. The original triangular grid of surface detectors with a 1500 m spacing is sensitive to cosmic-ray energies above $\sim 10^{18.5}$ eV [11]. Later, two denser arrays with 750 m and 433 m spacings were deployed to extend the energy range of the observatory to $\sim 10^{16.5}$ eV. The underground muon detector, which is of interest in the present work, consists of scintillators deployed next to the water Cherenkov detectors that constitute these denser arrays [7]. At each position, three 10 m^2 modules are buried at a depth of 2.3 m to shield electromagnetic particles [12].

IceCube, located at the geographic South Pole, is a cubic-kilometer Cherenkov detector, fundamentally designed as a neutrino observatory [8]. Complemented by its surface array IceTop, situated at an altitude of 2835 m, it extends its capabilities to cosmic ray physics. IceTop consists of a 1 km^2 array with 162 water Cherenkov detectors in 81 stations with a 125 m spacing. It measures the electromagnetic component and predominantly low-energy muons from extensive air showers generated by cosmic rays exceeding 10^{14} eV. High-energy muons are detected in coincidence in the in-ice detector IceCube.

Finally, the KASCADE Experiment was located at the Forschungzentrum Karlsruhe in Germany at an altitude of 110 m a.s.l. [9, 13]. It consisted initially of an electromagnetic and muon detector array upgraded to KASCADE-Grande by extending the array area to detect cosmic rays with energies between 10^{14} eV and 10^{18} eV. The muon detector component, which is of interest for this work, encompassed 252 detector stations arranged on a rectangular grid with a spacing of 13 m covering an area of 0.04 km^2 with plastic scintillators of $90\times90\times3$ cm^3 with 10 cm lead and 4 cm iron shields.

To shed light on the muon puzzle, improving the air shower simulation frameworks and enhancing their technical capabilities to integrate new theoretical models is of utmost importance. In this work, we present advancements in these aspects: we introduce a software extension in Sec. 2 to improve computing times, enabling the massive simulation of ultra-high energy showers in 3D. Then, in Sec. 3, we use this extension to compare muon-related air shower observables for different experiments. Finally, in Sec. 4, we discuss the impact on the muon content of air showers after a theoretical model modification based on the core-corona approach [14].

2 Air shower simulation framework: CONEX option in CORSIKA

The interpretation of cosmic-ray data has historically relied on Monte Carlo simulations that provide a detailed description of the air shower development. As the primary cosmic ray energy increases, the number of particles in the shower also increases, making these simulations computationally expensive, even with boost techniques such as the *thinning algorithms* THIN and THINMAX implemented in the CORSIKA framework [15]. Here, we group particles produced in an interaction with energy below a predefined threshold. From each group, only a randomly selected particle's evolution is simulated and stored. We account for energy conservation by assigning an appropriate weight to the products of this particle (the inverse

of the energy fraction taken by this particle) and stop the thinning process when a maximum weight is reached. The THINMAX algorithm further optimizes computation by putting priority on maximizing the weight over strict energy conservation, thus leading to a lower number of particles but with the same predefined maximum weight. To improve this situation even more, the air shower simulation software CONEX employs a hybrid approach [16], combining Monte Carlo treatment of high-energy particles (similar to the CORSIKA framework) with a numerical description of low-energy showers based on solving cascade equations [17–21]. This hybrid method improves computational efficiency and allows for more simulation repetitions, making CONEX more suitable for testing modifications of hadronic properties.

Describing extensive air showers requires two systems of cascade equations: one for the hadronic component and another for the electromagnetic component. In CONEX's hadronic equations, we consider only the so-called *projectile particles*, which include protons, neutrons, charged pions, and kaons. Projectile-air interactions produce *secondary particles* such as protons, neutrons, pions, kaons, photons, muons, and electrons. Other hadrons produced by decaying particles or through interactions are assumed to decay immediately into these secondary particles. Photons and electrons, once created, are directly transferred to the electromagnetic equations.

2.1 CONEX

In the CONEX framework, the cascade initiated by the primary hadron is simulated through explicit Monte Carlo until the produced secondaries reach an upper energy threshold. We fill all the sub-threshold particles into the *source terms* of the cascade equations, which give the initial conditions for the numerical analysis. Then, we solve the hadronic and electromagnetic cascade equations for each depth level. The spectra that result from the n^{th} level feed the source term of the $(\mathrm{n}+1)^{\mathrm{th}}$ level. Hadronic and electromagnetic particles are added to their respective source terms, regardless of the shower component from which they originate.

The hadronic cascade equations take into account all the possible processes in the following system of integro-differential equations:

$$\begin{aligned}\frac{\partial h_a(E,X)}{\partial X} = &-\frac{h_a(E,X)}{\lambda_a(E)} - \frac{h_a(E,X)}{\tau_a(E)\,\rho_{\mathrm{air}}(X)} + \frac{\partial}{\partial E}\left(\beta_a^{\mathrm{ion}}(E)\,h_a(E,X)\right)\\ &+ \sum_d \int_E^{E_{\max}} dE'\, h_d(E',X)\left(\frac{W_{d\to a}(E',E)}{\lambda_d(E')} + \frac{D_{d\to a}(E',E)}{\tau_d(E')\,\rho_{\mathrm{air}}(X)}\right)\\ &+ S_a^{\mathrm{had}}(E,X),\end{aligned} \tag{2.1}$$

where $h_a(E,X)$ is the differential energy spectrum of the hadron type a, with energy E at depth position X along a given straight line trajectory. $\beta_a^{\mathrm{ion}} = -dE_a/dX$ is the ionization energy loss per depth unit, $\lambda_a = m_{\mathrm{air}}/\sigma_{\mathrm{inel}}^{a-\mathrm{air}}$ the mean free path, and τ_a the lifetime in the laboratory system (related to the proper lifetime by $\tau_a = \tau_a^0 E/m_a$). m_{air} and m_a are the average mass of an air molecule and the mass of hadron type a, respectively, while $\sigma_{\mathrm{inel}}^{a-\mathrm{air}}$ is the inelastic cross section of an interaction between this hadron type and an air molecule. $W_{d\to a}$ and $D_{d\to a}$ are the inclusive secondary spectra for interactions and decays, respectively. Muons are treated as hadrons but don't have interaction terms. The five terms in Eq. 2.1 describe the variation in the hadron number due to interactions with air nuclei, particle decays, ionization loss, and hadron production from higher energy parents (with energies up to $E_{\max}$) and source terms. The particle decay term results from the decay rates $\mathrm{d}h_a = -h_a \mathrm{d}L/(\tau_a c)$

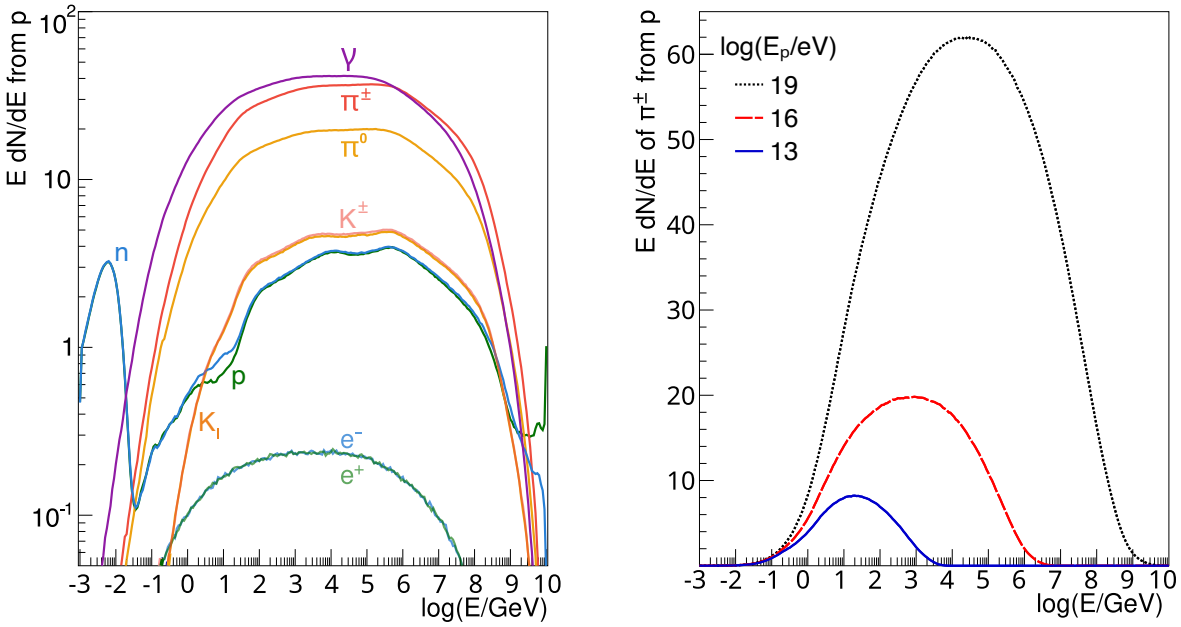

Figure 1: (Left) Energy spectra of secondary particles from p-air interactions at 10^{19} eV with EPOS LHC. Different colors denote different particle species. (Right) $\pi^{\pm}$ spectra from p-air interactions for different proton energies with QGSJETII.04.

and $\mathrm{d}L/\mathrm{d}X = \rho_{\mathrm{air}}^{-1}(X)$, where c is the speed of light and $\rho_{\mathrm{air}}(X)$ is the air density at depth X.

The source term $S_a^{\mathrm{had}}(E, X)$, defining the initial conditions, has three components:

$$S_a^{\mathrm{had}}(E, X) = S_a^{\mathrm{MC}\to\mathrm{had}}(E, X) + S_a^{\mathrm{em}\to\mathrm{had}}(E, X) + S_a^{\mathrm{em}\to\mu}(E, X). \tag{2.2}$$

The first term consists of all contributions of sub-threshold hadrons produced during the Monte Carlo simulation of above-threshold particles:

$$S_a^{\mathrm{MC}\to\mathrm{had}}(E, X) = \sum_i \delta_{d_i}^a \; \delta(E - E_i) \; \delta(X - X_i), \tag{2.3}$$

with d_i, E_i, X_i being the type, energy, and depth position of the source particle i. The second term includes the hadrons coming from the photonuclear interactions in the electromagnetic cascade equations. The production distributions $W_{\gamma\to a}(E', E)$ are approximated at high energy with $\pi^{+/-}$-air interactions and at low energy with ρ^0 and ω resonances:

$$S_a^{\mathrm{em}\to\mathrm{had}}(E, X) = \int_E^{E_{\max}} dE' \; l_\gamma(E', X) \; W_{\gamma\to a}(E', E) \; \tilde{\sigma}_\gamma^{\mathrm{photonuclear}}(E'), \tag{2.4}$$

where l_γ is the photon energy spectrum. Finally, the photoproduction of muon pairs gives rise to the last contribution in the hadronic source term:

$$S_a^{\mathrm{em}\to\mu}(E, X) = \int_E^{E_{\max}} dE' \; l_\gamma(E', X) \; W_{\gamma\to\mu}(E', E) \; \tilde{\sigma}_\gamma^{\mu-\mathrm{pair}}(E'). \tag{2.5}$$

Analogously, the electromagnetic equations apply to electrons, positrons, and photons. The equally weighted interaction processes considered are Bremsstrahlung, Bhabha, Moeller,

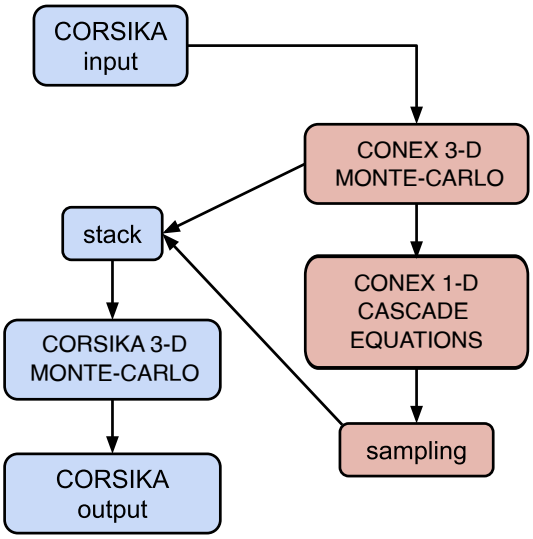

Figure 2: Flow chart of the CONEX option in CORSIKA. The CORSIKA structure manages the steering files that set the simulation parameters and transfers these to begin the Monte Carlo simulation in CONEX. CONEX uses cascade equations to handle particles with energy below a predefined threshold. CORSIKA recovers then secondaries from the Monte Carlo or cascade equations with energy below a second threshold and treats them again with 3D Monte Carlo. From the solutions of the cascade equations, individual particles are sampled and saved into the CORSIKA stack.

pair annihilation, and pair production with no decay term. This approach allows a partial analytical solution using eigenvalues in contrast to the pure numerical solution of the hadronic equations [16].

CONEX implements the Monte Carlo simulations with the updated high-energy hadronic interaction models EPOS LHC [22], QGSJetII.04 [23], and SIBYLL 2.3d [24]. In the numerical analysis, the same models are used to pre-calculate the spectra of secondary particles $W_{d\to a}$: for each model, secondary particle type, projectile particle type, and projectile energy, CONEX provides one spectrum. The projectile energy is discretized in 20 logarithmic energy bins per decade from 10^9 eV to 10^{19} eV, which results in $\sim 10^4$ secondary particle spectra. For example, Fig. 1 left panel shows all the EPOS LHC energy spectra of secondary particles resulting from an interaction between a 10^{19} eV proton and an air molecule. Fig. 1 right panel shows the charged pion energy spectra from proton-air interactions for three different proton energies with QGSJetII.04: 10^{13} eV (solid-blue line), 10^{16} eV (dashed-red line), and 10^{19} eV (dotted-black line). Modifying these spectra can effectively change the properties of the hadronic interactions used in air shower simulations.

2.2 Extension to multi-dimensional distributions

CONEX only provides the energy distributions of all particles along the shower axis, which allows fast and realistic 1-dimensional simulations of the longitudinal distribution, which describes the shower development as a function of atmospheric depth. To obtain 3-dimensional (3D) distributions of particles at the ground, CONEX has been included in the CORSIKA package [25] as depicted in Fig. 2. In this integration, the numerical analysis returns to Monte Carlo tracking when particles fall below a second energy threshold [20]. Now, we propagate in 3D particles produced in the cascade equations that fall below this threshold and high-energy particles simulated in the initial CONEX Monte Carlo part.

We select the second transition threshold by balancing computation time with accuracy: the threshold must be low enough to reduce the Monte Carlo contribution but high enough to avoid biases. At the highest energies, the longitudinal momentum is orders of magnitude higher than the typical $\lesssim 10$ GeV transverse momentum, and the emission angle along the shower axis is small. Consequently, at a few TeV, we can neglect this angle [20], and CONEX's cascade equations will accurately describe the shower development. To further

reduce this threshold, we compute the mean transverse momentum of the secondary particles using the cascade equations, thus decreasing the transitions to Monte Carlo when emission angles become significant. Since CONEX solves the equations at consecutive depth levels, this procedure results in a (1+1)D way of describing the air shower development.

In the cascade equations, we compute the secondary particles' mean transverse momentum, assuming a realistic angular distribution instead of a bare longitudinal propagation. To track the properties of each hadronic interaction model, the $\langle p_{\rm t}^2 \rangle$ are tabulated in $T_{d\to a}$ spectra (T^W for interaction terms and T^D for decay terms) for each projectile energy, projectile particle and hadronic interaction model, as a function of the secondary particle type and energy. Thus, we can write another set of cascade equations for hadrons and muons that describe the accumulation of transverse momentum:

$$\begin{aligned}\frac{\partial p_{{\rm t}a}^2(E,X)}{\partial X} =& \sum_d \int_E^{E_{\rm max}} dE'\; h_d(E',X) \\ & \left(\frac{W_{d\to a}(E',E)}{\lambda_d(E')} \; \left[T^W_{d\to a}(E',E) + C_a\left(\langle p_{{\rm t}d}^2(E',X)\rangle, E'\right)\right] \right. \\ & \left. + \frac{D_{d\to a}(E',E)}{\tau_d(E')\;\rho_{\rm air}(X)} \; \left[T^D_{d\to a}(E',E) + C_a\left(\langle p_{{\rm t}d}^2(E',X)\rangle, E'\right)\right] \right) \\ & + S_a^{p_{\rm t}^2}(E,X). \end{aligned} \tag{2.6}$$

Using that $\langle p_{\rm t}^2(E,X)\rangle = p_{\rm t}^2(E,X)/h(E,X)$, we add the $\langle p_{\rm t}^2\rangle$ of a previous generation via a correction function C_a for a particle a. We use this function to fine-tune $\langle p_{\rm t}^2\rangle$ in the cascade equations based on Monte Carlo simulations. Of all hadrons, only the last generation has made a significant contribution. Thus, we can neglect the transverse momentum of generations beyond the last one ($C_a \equiv 0$ in those cases). For muons whose main contributions come from the decay of pions and kaons, we account for $\langle p_{\rm t}^2\rangle$ via

$$C_\mu(\langle p_{\rm t}^2\rangle, E) = \max\left(0.4\;\langle p_{\rm t}^2\rangle + \frac{\langle p_{\rm t}^2\rangle^2}{E\;(E+2m_\mu^2)}, 0\right), \tag{2.7}$$

where $(E+2m^2)E = P^2$ is the total momentum since E is the kinetic energy. Particles are sampled following a (Moyal + Normal) distribution using $\langle \sin^2(\theta)\rangle$ and $\langle \sin^2(\theta)\rangle^2$ as parameters:

$$\begin{aligned} f(x,\mu,\sigma) =& \frac{1}{2}\;\frac{\exp\left[-\frac{1}{2}\left(\frac{\mu-x}{\sigma} + e^{-\frac{\mu-x}{\sigma}}\right)\right]}{\sigma\sqrt{2\pi}} \\ & + \frac{1}{2}\;\frac{\exp\left[-\frac{1}{2}\frac{(\mu-x)^2}{2\sigma^2}\right]}{\sigma\sqrt{4\pi}}, \end{aligned} \tag{2.8}$$

with $\mu(a,b) = \log_{10} a - 0.5\sigma^2(a,b)$ and $\sigma^2(a,b) = 0.5\log_{10}(1+b/a^2)$, where $a = \langle \sin^2(\theta)\rangle$, $b = \langle \sin^2(\theta)\rangle^2$, and $\langle \sin^2(\theta)\rangle$ is given by $\langle p_{\rm t}^2\rangle / P^2$. In Fig. 3, we show the angular distributions from this procedure and Monte Carlo simulations, which are consistent.

In this approach, we set a 1 TeV low-energy threshold for transferring hadrons from CONEX to CORSIKA's tracking system, ensuring an accurate description of the particle number as a function of distance from the shower core, commonly referred to as the lateral distribution function. To track muons in the Earth's magnetic field, we transfer them from

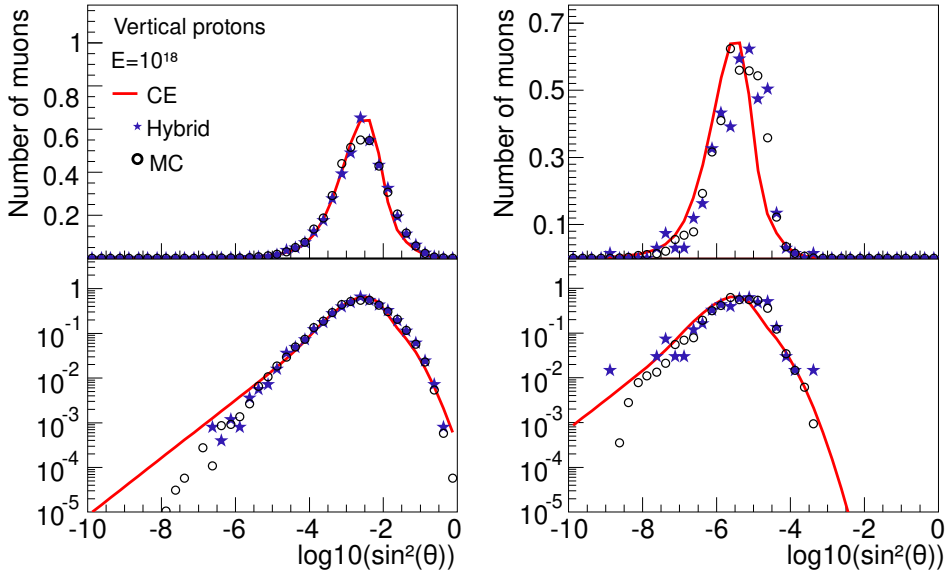

Figure 3: Normalized muon angular distributions for a proton-initiated shower with energy $E_0 = 10^{18}$ eV using QGSJET-01, where θ is the angle between the muon direction and the shower axis. Red lines represent the distribution from the cascade equations, and blue stars are muons sampled from the corresponding cascade equations in CONEX. Open circles are the result of pure Monte Carlo simulations. (Top) Linear scale. (Bottom) Logarithmic scale. (Left) Muons with energy around 5 GeV. (Right) Muons with energy around 180 GeV.

the CONEX Monte Carlo directly to CORSIKA Monte Carlo and systematically sample them back from the cascade equations to the CORSIKA Monte Carlo at each step (every 10 g/cm^2).

We sample the electromagnetic particles from the solutions of the cascade equations to be processed by the CORSIKA Monte Carlo following the same process. However, since the Coulomb interaction determines the scattering angle, we decompose this potential into higher-order moments and analytically compute the cascade equations at each slant depth step. The second moment allows the computation of $\langle \cos^2(\theta) \rangle$, from which we extract $\langle \sin^2(\theta) \rangle = 1 - \langle \cos^2(\theta) \rangle$, leading to an increase of the short computational time for the cascade equation resolution by solely a factor of two [26, 27]. We set the transition threshold for electromagnetic particles to a kinetic energy of 10 GeV. While muons and hadrons can propagate large

Parameter	KASCADE	IceTop	Auger
Primary energy [$\log_{10}$(E/eV)]	16	17	19
Zenith angle [°]	0-27-41-53-67	0-27-41-53-67	0-27-41-53-67
Altitude [m]	150	2800	1450
Optimal distance from core d [m]	100-200	400-500	1000-1100
Muon energy threshold $E_{\rm th}$ [MeV]	230	200	300
Number of showers	240	240	90

Table 1: Air-shower and simulation parameters used in the simulation library.

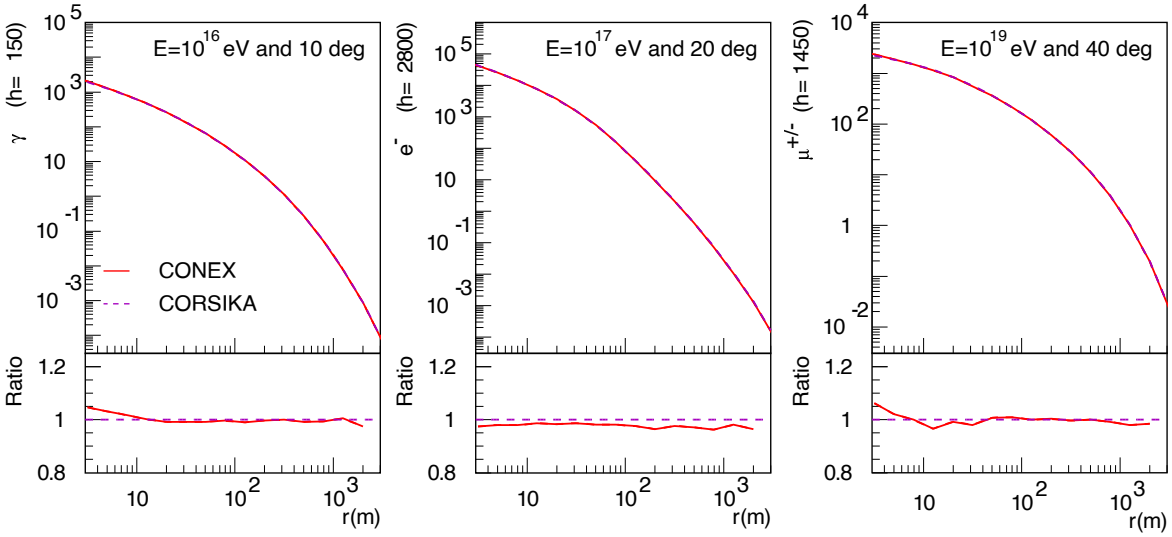

Figure 4: Lateral distribution functions (top) for proton-initiated showers using CORSIKA and CONEX 3D (EPOS LHC), together the ratio between models (bottom). (Left) photons for KASCADE, (middle) electrons for IceTop, (right) muons for Auger.

distances, electromagnetic particles are strongly attenuated. To avoid sampling particles absorbed before reaching the ground, we define the minimum vertical depth (or height above the observation level) below which we track electromagnetic particles. Particles remain in the cascade equations above this cut, by default 400 g/cm^2, but can still produce low-energy hadrons or muons.

To validate the new framework, we compare CORSIKA and CONEX 3D simulations

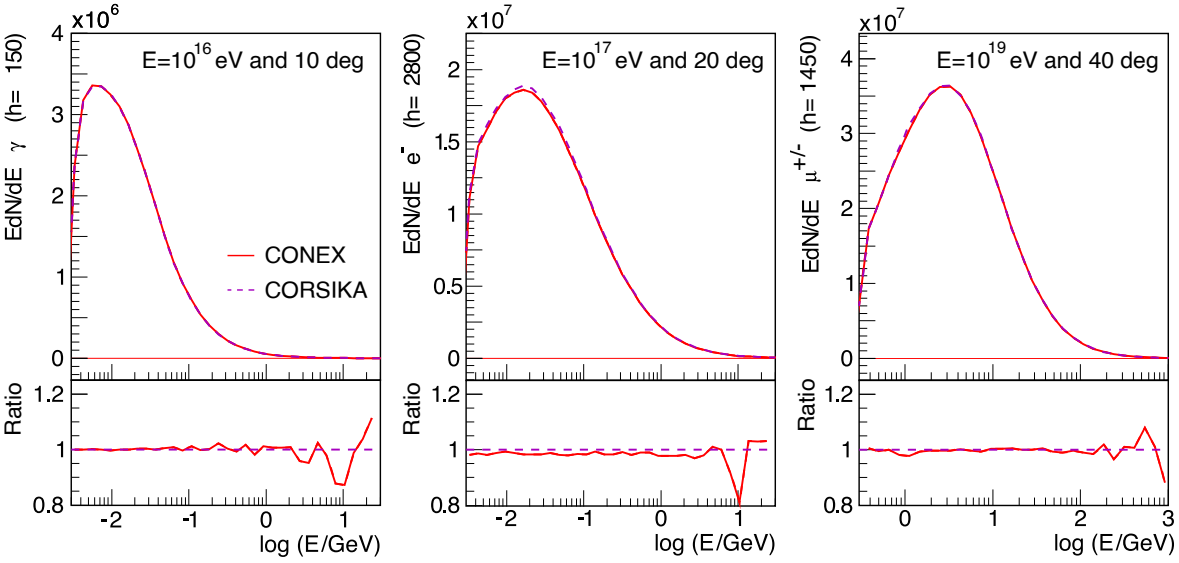

Figure 5: Mean energy spectra (top) obtained with CORSIKA and CONEX 3D (EPOS LHC), and their corresponding ratios (bottom). (Left) photons for KASCADE, (middle) electrons for IceTop, (right) muons for Auger.

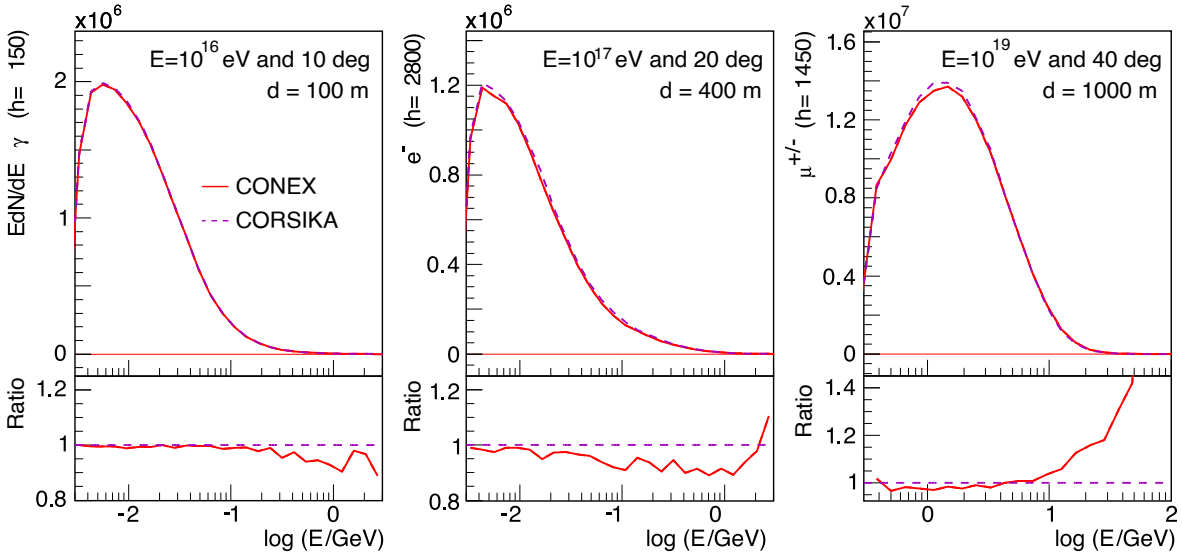

Figure 6: Energy spectra for proton primary showers at each experiment's optimal distance (top) with CORSIKA and CONEX 3D (EPOS LHC), and their corresponding ratios (bottom). (Left) photons for KASCADE, (middle) electrons for IceTop, (right) muons for Auger.

for three configurations representative of the main current experiments. We summarize in table 1 the respective cosmic ray primary energy and zenith angles considered, together with the altitude above sea level, the muon energy threshold, and the optimal distance to the shower core appropriate for each experiment. We selected the muon energy threshold in KASCADE based on the minimum energy required to penetrate the detector shield [9]. For Auger and IceTop, we determined the muon energy threshold by considering their energy distribution and experiment altitude, ensuring it is sufficiently low to capture most particles (see Figure 12). Similarly, for electromagnetic particles, we used a threshold of $E_{\rm th} = 3\,\mathrm{MeV}$. We measure a particle's distance to the shower core in the detector plane.

Figs. 4,5, and 6 display the mean lateral distribution functions, the energy spectra over all distances from the shower core, and the energy spectra at the optimal distance from the core, respectively. In each, the left panel corresponds to the photon distribution (γ) at the ground for the KASCADE experiment, the middle panel to electrons in IceTop, and the right panel to muons at the Pierre Auger Observatory. Dashed lines labeled "CORSIKA" refer to simulations of single-proton initiated showers with only Monte Carlo, and solid lines labeled "CONEX" refer to simulations with cascade equations at intermediate energy. Since we use the same seeds for the high-energy Monte Carlo, the showers have the same global evolution (same $X_{\rm max}$) and can be directly compared at ground level.

In Fig. 4, the mean ratio of the muon lateral distribution functions is close to one, with minor discrepancies ($< 5\%$) at less than 10 m of the shower core, a distance not relevant for most of the high-energy shower experiments, or in IceTop, that measures showers close to their maximum. We note a slight underestimation of electromagnetic particles near the shower maximum (IceTop), which is limited to a percent level. CONEX accurately reproduces the muon energy spectrum across the entire energy range, as demonstrated in Fig. 5. At larger distances from the shower core (400 m and 1000 m), as shown in Fig. 6, the energy spectra exhibit more significant discrepancies, particularly an excess of high-energy muons in the CONEX simulations. Nevertheless, the peak is well-reproduced, and the high-energy tail has

	KASCADE		IceTop		Auger	
	[min]	[MB]	[min]	[MB]	[min]	[MB]
CORSIKA+THIN	35	35	40	304	237	732
CORSIKA+THINMAX	21	20	25	160	210	620
CONEX 3D	14	24	24	178	22	95

Table 2: Computing times (in minutes) and file sizes (in megabytes) for one proton air shower simulation with CORSIKA, with the THIN, THINMAX or CONEX 3D option, considering the detector configurations of the KASCADE Experiment ($E_0 = 10^{16}$ eV, zenith angle 15°), the IceTop Experiment ($E_0 = 10^{17}$ eV, zenith angle 20°) and the Pierre Auger Observatory ($E_0 = 10^{19}$ eV, zenith angle 40°). Optimal thinning (see text) and the hadronic interaction model SIBYLL 2.3D are used here.

minimal impact on experimental results. Photons, electrons, and muons behave equally for the three tested phase spaces.

In Table 2, we summarize the computing times and file sizes for CORSIKA+THIN [28], CORSIKA+THINMAX [28], and CONEX 3D simulations, using the SIBYLL 2.3D hadronic interaction model. We use an optimal thinning in the CORSIKA simulations: a thinning threshold given by the fraction $E_{\rm thr} = 10^{-6}$ for electromagnetic particles, a maximum weight defined as $W_{\rm max} = E_0 \times E_{\rm thr}$ with 100 times lower values for hadrons and muons. The THINMAX option has also been tested but applies only to electromagnetic particles. With this option, the thinning process is allowed to violate the energy conservation (small on average) to allow all electromagnetic particles to reach exactly $W_{\rm max}$, thus improving the computation time and disk occupancy by about 30% and 50%, respectively. In the Auger case, this improvement is less significant because the simulation spends more time calculating the hadronic shower, while only the electromagnetic shower is affected by THINMAX.

The CONEX 3D option uses the same value $W_{\rm max}$ to sample the particles from the cascade equations. This results in a very peaked weight distribution at the maximum weight, both for electromagnetic particles and muons. Consequently, there are fewer particles tracked in the Monte Carlo. Thus, the simulation time and disk space can be reduced from a factor of 2 at low energy to a factor of 10 at high energy while preserving the accuracy of the results. At large distances from the core, where there are fewer particles, this can introduce large statistical fluctuations. We can reach the statistics needed while keeping reasonable simulation times by reducing $W_{\rm max}$ for muons and hadrons. As an example, in the Auger case, if we reduce the value of $W_{\rm max}$ (in CONEX) for electromagnetic particles and hadrons by a factor of 10, the computation time is still lower than for CORSIKA by about 30%, while the statistics at the ground is much larger (less artificial fluctuations). In contrast, there is no considerable difference between CONEX 3D and THINMAX in IceTop since $W_{\rm max} = 1$ for hadrons and muons. Then, the propagation stops at the maximum of the shower, and using the cascade equations does not reduce the computing time. The CONEX 3D option is convenient for high-energy or inclined showers.

2.3 Simulation library

The simulation library in this work consists of three groups representing the main air shower experiments at each altitude (see Sec. 1). For each group, we run simulations using

parameters specific to the corresponding setting. In contrast, the CONEX parameters aim at avoiding 3D Monte Carlo simulations at high energies and produce "mean" showers without fluctuations from the first interaction. To increase statistics in phase space regions with a low number of particles (high energies and large distances from the shower core), we run several simulations with the same parameters, which result in the same mean shower characteristics but with fluctuations due to the randomness in the sampling step (see explanation to Fig. 2). In this study, we present averages from the whole set of simulations.

The Auger set comprises 90 mean proton air showers, while IceTop's and KASCADE's have 240. For each set, we simulate five different zenith angles with the same weight: $\sin\theta$: 0°, 27°, 41°, 53° and 67°. We use the shower plane to count particles (projection from the observation plane to the plane perpendicular to the core propagation) and analyze the distance ranges of $d = 1000 - 1100\,\mathrm{m}$ for Auger, $d = 400 - 500\,\mathrm{m}$ for IceTop and $d = 100 - 200\,\mathrm{m}$ for KASCADE. We perform the simulations using CORSIKA's version v77410, which has CONEX v7.5 implemented. In addition, we use the last hadronic interaction models in each set: EPOS LHC, QGSJetII.04, and SIBYLL 2.3d. In Table 1, we summarize the simulation parameters for each air shower experiment and the number of simulations for each set, along with the muon energy thresholds and the d values.

3 Muon-related observables with CONEX

To better understand the behavior of muons in extensive air showers, we analyze the number of particles in the shower as a function of the traversed overburden, referred to as the longitudinal profile. In Fig. 7, we present longitudinal profiles of all particles (left panel) and muons only (right panel), normalized to a maximum value of 1, for proton showers with different incidence angles and primary energy $E_0 = 10^{18}\,\mathrm{eV}$, using EPOS LHC for the high-energy interactions. Electromagnetic particles dominate the all-particle distributions but have a very strong attenuation after the shower maximum. Thus, after around $1500\,\mathrm{g/cm^2}$ (corresponding to the sea-level for a zenith angle of 55°), this component becomes negligible (it then only stems from the decay of muons into electrons and positrons). In contrast, muon profiles have a slow attenuation allowing their detection at ground even for very inclined

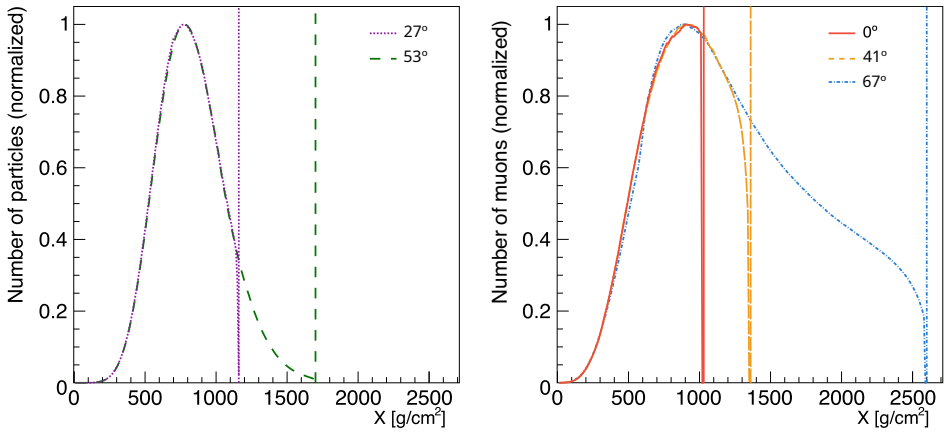

Figure 7: Normalized longitudinal profiles of all particles (left) and muons only (right) for proton showers with a primary energy of $E_0 = 10^{18}\,\mathrm{eV}$ and different zenith angles. We used EPOS LHC as hadronic interaction model.

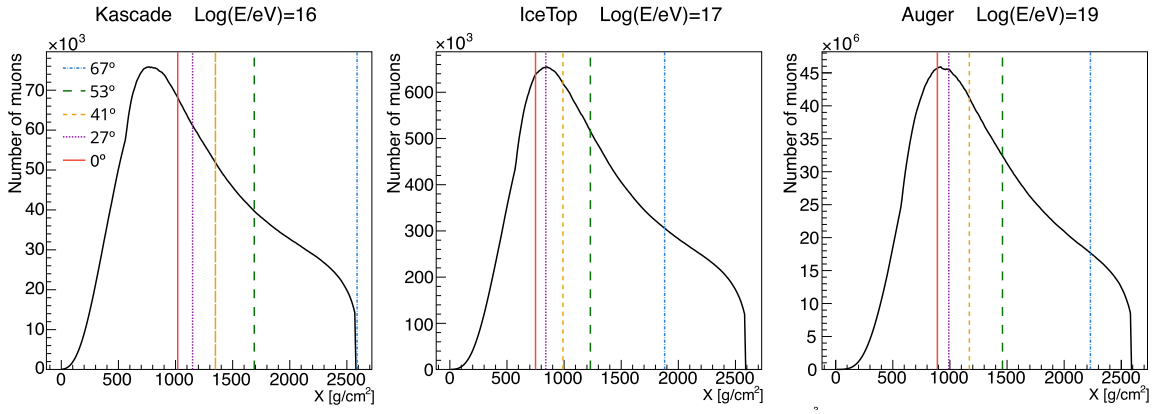

Figure 8: Muon longitudinal distribution at sea level for proton-initiated showers with an incidence angle of 67°) using EPOS LHC. (Left) KASCADE, (middle) IceTop, and (right) Auger energies. The vertical lines show the position of the ground for each site for different zenith angles.

showers. Another effect is observed in the muon profiles: a fast but smooth drop before reaching the ground. This effect is more pronounced for large zenith angles due to geometry. Particles far from the core tend to reach the ground before those near the core since we analyze particles at the shower plane and thus are accounted for in the final profile at smaller depths than those near the core. For the same reason, the earlier this effect sets in, the more inclined the shower is.

We show in Fig. 8 the number of muons as a function of the shower depth for proton showers at 67°) down to sea level, indicating with vertical lines the depths at which the showers hit the ground for different primary incidence angles and experimental sites (different heights). The left panel represents results for the KASCADE scenario, the middle for IceTop, and the right for Auger. Each experiment measures different stages of shower development. KASCADE detects showers for all zenith angles after $N_\mu^{\max}$, while at Auger, vertical showers reach the maximum number of muons close to the ground. IceTop can detect showers before and after the value of $N_\mu^{\max}$ is attained, depending on the inclination of the shower.

In Fig. 9, we present the muon lateral distribution (top), which is the muon density

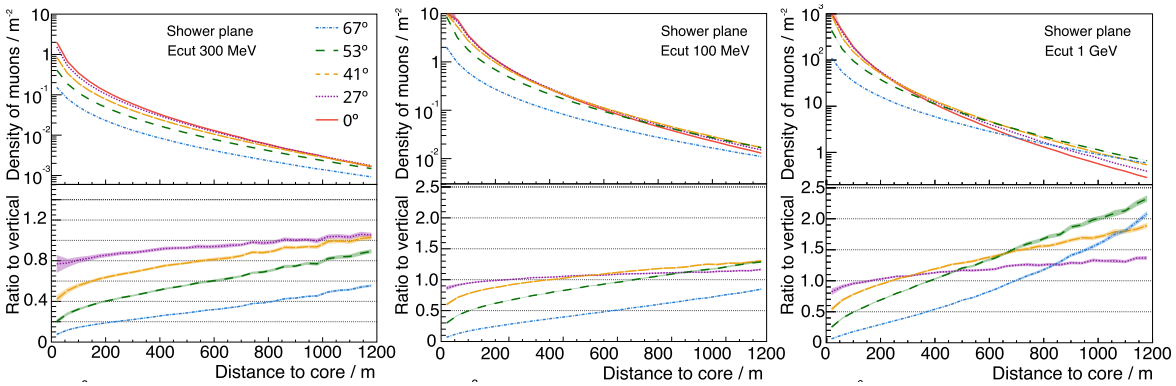

Figure 9: Muon lateral distribution for proton-initiated showers with different incidence angles using EPOS LHC. (Left) KASCADE, (middle) IceTop, (right) Auger.

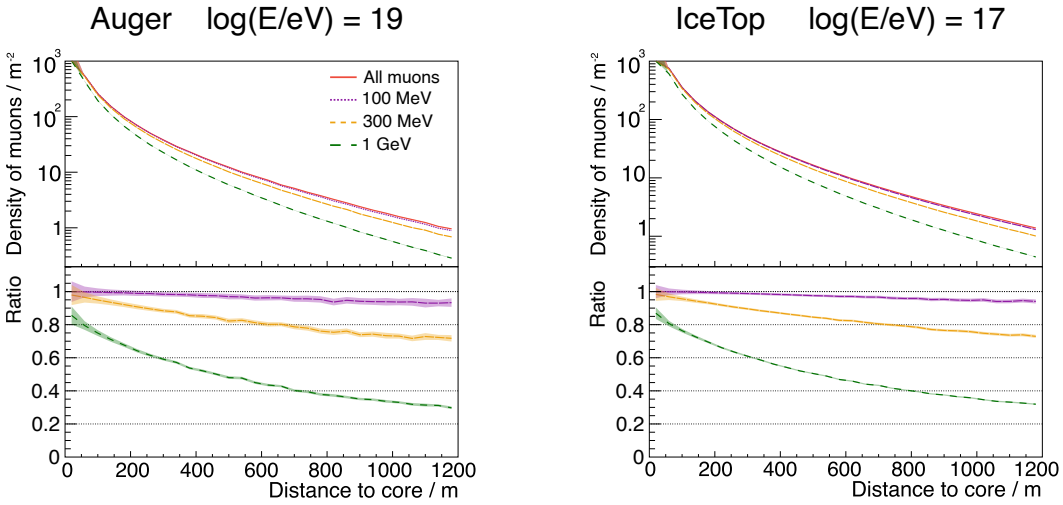

Figure 10: Muon lateral distribution functions for proton-initiated showers with EPOS LHC at the Pierre Auger Observatory (left) and the IceTop array (right). We show simulations of vertical showers ($\theta = 0°$) for different muon energy thresholds with the ratio between the lateral distribution for muons with energy above the threshold and all muons.

as a function of the distance to the shower core, for different experiments and zenith angles and the ratio between muon densities for an inclined incidence angle and vertical showers (bottom). As the zenith angle increases, the muon density tends to decrease due to the attenuation caused by the increased amount of matter traversed. Concurrently, the distance from the points of production of the particles along the axis to the ground increases with the incidence angle, leading to a flatter shower front. Consequently, the muon density ratio between inclined and vertical showers rises with the distance from the shower core. In the KASCADE scenario, the muon density of showers with $\theta = 27°$ is higher than for vertical showers beyond 900 m. For IceTop, the muon density for vertical showers is most significant, only close to the shower core. This effect is produced by the higher altitude of the array (see Fig. 8). In this case, we observe an earlier stage of the shower development, and low-energy muons with larger scattering angles are not yet attenuated, contributing to higher ratios compared to KASCADE.

To further understand the difference between the muon lateral distribution functions, we present in the left panel of Fig. 10 the muon density as a function of the distance to the shower core of proton-initiated vertical showers with different muon energy thresholds for the Auger (left) and IceTop (right) scenarios, along with the ratio between the lateral distributions for muons with energy above the threshold and all muons. We can infer that the dependence of muon energy on the distance from the shower core from the ratio decreases with the energy threshold and distance to the core. The similarity between Auger and IceTop denotes that this effect dominates the lateral distribution shaping in Fig. 9 over other differences in the experiments.

In Fig. 11, we present the muon energy spectra at a characteristic distance from the shower core (see Sec. 2.3) for each experiment. The position of the peak shifts to higher energies as the angle of incidence increases, mainly because the atmosphere attenuates lower-energy muons. In addition, since inclined showers develop in a less dense atmosphere, the distance between interaction points is larger than the decay length at advanced shower stages.

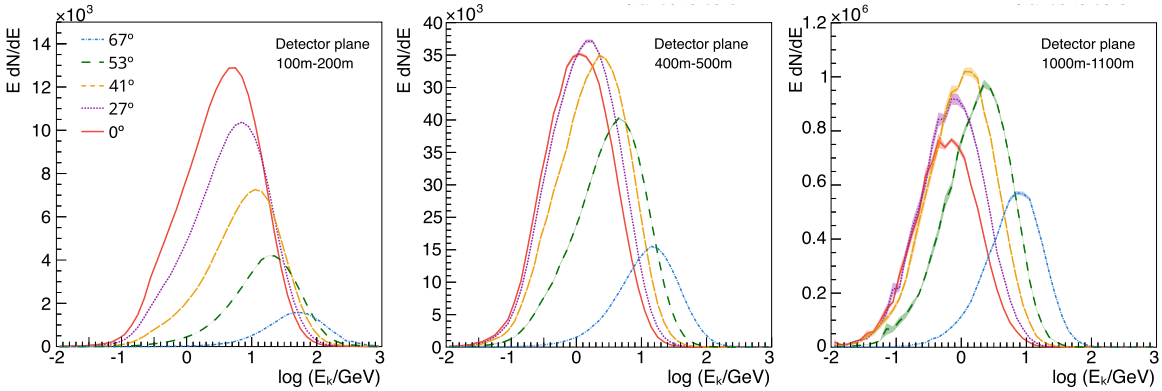

Figure 11: Muon energy spectra for proton-initiated showers with different incidence angles using EPOS LHC. (Left) KASCADE, (middle) IceTop, (right) Auger.

Then, the critical energy at which kaons and pions decay into muons increases. Consequently, the energies of the muons "shift" to higher values as the incidence angle increases.

Furthermore, since KASCADE measures showers after $N_\mu^{\max}$, the number of particles (or height of the distribution peak) decreases with the zenith angle, again as a result of attenuation. However, this behavior is not present in Auger and IceTop. To better understand these differences, we present in Fig. 12 the energy spectra for the same set of simulations (10^{19} eV proton showers simulated with EPOS LHC at Auger) at the radial distances of 100-200 m (left), 400-500 m (center) and 1000-1100 m (right). Since spectra for different experiments at the same radial distance are similar, the leading effect on the shaping of the muon energy spectra comes from the measurement at different distances from the shower core. As said, the lateral spread of the muons is increasing with the incidence angle, causing the position of the peak of the number of muons to be deeper with the increase of the radial distance. As a consequence, depending on the incidence angle, IceTop and Auger may measure shower stages before or after $N_\mu^{\max}$, thus giving a not monotonic behavior of the muon number with the zenith angle.

Finally, Fig. 13 shows the simulated muon energy spectra for proton showers at the

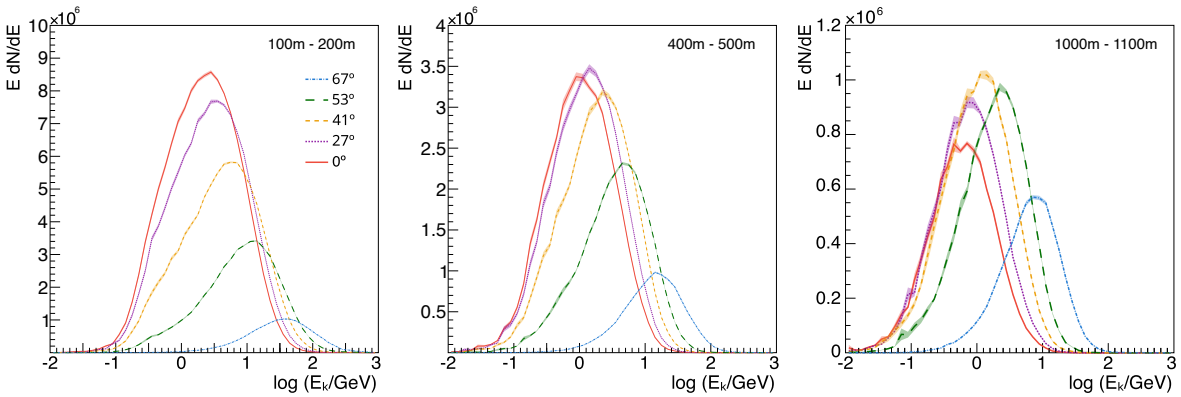

Figure 12: Muon energy spectra at different distances from the shower core and for different zenith angles, as predicted from EPOS LHC simulations of 10^{19} eV proton showers at the Pierre Auger Observatory.

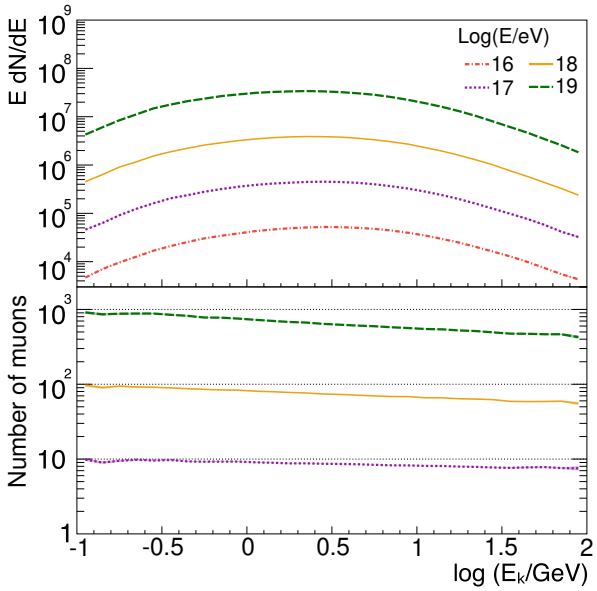

Figure 13: Muon energy spectra for different proton shower energies (top) and the corresponding ratio to the lowest energy (bottom), using EPOS LHC simulations. We show showers at the Pierre Auger Observatory and with an incidence angle of 41°.

Pierre Auger Observatory with an incidence angle of 41° and different primary energies. The ratios between the energy spectra at a given energy and 10^{16} eV are almost linear to the muon energy with a small negative slope. At high energies, muons are mainly decay products of mesons created in hadronic interactions. We can model this number of muons as $(E_0/\xi_c^\pi)^\beta$ [2], where E_0 is the primary energy, ξ_c^π is the pion critical energy and β is a parameter with a value close to 0.9 [1]. This model accurately describes the factor of about 10^β at high muon energies between consecutive spectra. At lower muon energies, the photonuclear effect plays a dominant role [29]. Here, a photon interacts with a nucleus in the atmosphere and creates a μ^+-μ^- pair or some hadron or meson that subsequently decays into a muon. Since the number of photons is directly proportional to the primary energy, these type of muons are then linearly dependent on the primary energy, too (ratio is 10 for a 10 fold increase of the energy). For this reason, the gap between spectra decreases as the muon energy increases.

Since the number of muons in air showers constitutes a parameter that is sensitive to the primary cosmic-ray composition, simulations are crucial to determine the relation between muon density and cosmic-ray composition and then interpret the muon content in data. At each experiment, the ratio between the number of muons for iron- and proton-induced air showers depends on the incidence angle, distance to the shower core, and muon energy.

In the left panel of Fig. 14, we show the longitudinal profiles of 10^{17} eV proton (solid lines) and iron (dashed lines) showers as simulated for KASCADE and considering different incidence angles, along with the corresponding iron-to-proton ratios. For a fixed experiment altitude, different stages of the shower development are measured (represented by vertical dotted lines in the figure), depending on the incidence angle, which leads to different ratios between proton and iron.

In the right panel of Fig. 14, we present the ratio of EPOS LHC muon lateral distribution functions for iron and proton showers, averaged over all zenith angles (with weights

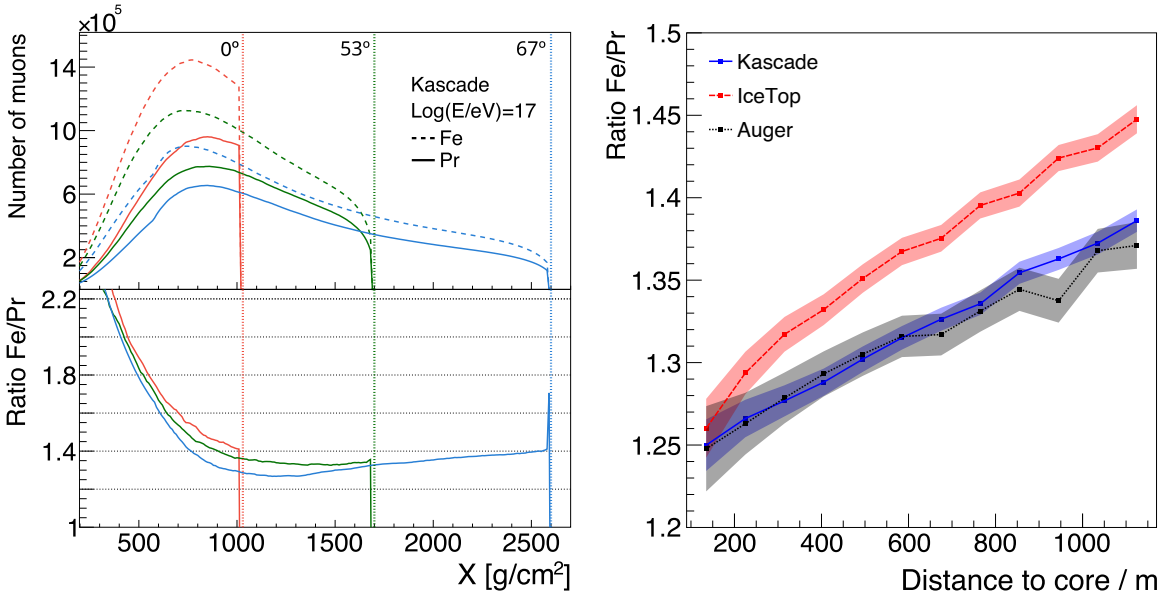

Figure 14: (Left) Longitudinal profiles of proton- and iron-initiated showers (top) and the corresponding iron-to-proton ratios (bottom) for showers of 10^{17} eV primary energy at various incidence angles as predicted for KASCADE. (Right) Ratios of muon lateral distribution functions for iron and proton showers from different experiments, averaged over all zenith angles and weighted by the respective solid angles. Both figures are based on simulations using EPOS LHC.

that correspond to the solid angle), for the three experiments. The increase in the ratio with distance from the shower core is due to a geometric effect: iron showers develop higher in the atmosphere and produce more muons farther from the core compared to proton showers at a given altitude. As the distance from the core increases, the muons that are detected originate from higher altitudes.

Finally, we assess the impact of both geometry effects in Fig. 15, where we display the ratio of the number of muons as a function of the incidence angle for each experiment and at different distances to the shower core. Generally, the ratio increases when measuring at higher altitudes, further from the shower core, and at smaller incidence angles. The ratio decrease for large zenith angles at Auger and IceCube results from measuring stages close to the shower maximum and muons of lower energy far from the shower core (see Fig. 12). The ratio increase for large zenith angles at KASCADE results from measuring higher muon energies (see Fig. 11, left). In addition, since iron showers develop in a less dense atmosphere, pions decay at higher energies, producing more high-energy muons than proton showers. Consequently, the ratio increases weakly with muon energy: in Auger, for example, the ratio is 1.15 for muons with 0.1 GeV and 1.7 for muons of 10 GeV.

4 Simplified core-corona model

CONEX, either in its stand-alone version or as an option in CORSIKA, implements the latest high-energy hadronic interaction models: EPOS LHC, QGSJETII.04, and SIBYLL 2.3D. The production of hadrons in these event generators is based on string fragmentation models and fails to reproduce muon-related observations (see Sec.1). Recent measurements at the

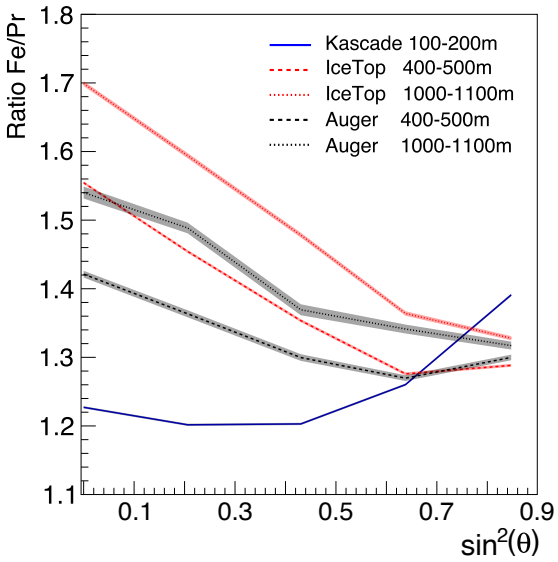

Figure 15: Ratio of the number of muons between iron and proton showers with a primary energy of 10^{17} eV (simulated using EPOS LHC), as a function of the incidence angle, at different experiments and distances from the shower core.

LHC hint towards the existence of other production mechanisms, such as collective statistical hadronization. This mechanism leads to an increase in the muon production in hadronic cosmic ray interactions [14, 30–32]. The core-corona model of heavy ions [33] combines both production mechanisms: the large-density region of interaction (core) hadronizes statistically, while the low-density region (corona) is modeled through string fragmentation.

The muon deficit in air shower simulations relates to the hadronic interaction model's representation of the energy distribution between electromagnetic particles and hadrons, expressed as $R = E_{\rm em}/E_{\rm had}$. The neutral to charged pion production ratio $\pi^0/\pi^\pm$ strongly impacts R, as muons mainly stem from charged pion decay, while neutral pions primarily feed the electromagnetic component. Hadronic interaction simulations implement different hadronization mechanisms to describe the particle population and final state energy, generating different R values.

Current hadronic interaction models use the string fragmentation model to describe hadronization processes, which accurately models electron-positron and low-energy proton-proton collisions. However, in heavy ion collisions, where energy densities are much higher, a fluid-like behavior with statistical hadronization is expected. This scenario favors the production of heavier particles, reducing the fraction of π^0 compared to other particle types, thereby lowering the R value.

This fluid-like behavior, referred to as collective effects, was observed in both heavy-ion collisions and in proton-proton collisions [34–40]. For heavy ions, the formation of a quark-gluon-plasma, described by the laws of hydrodynamics and followed by statistical decay, is modeled as a phase of parton matter where confinement is not required [41–43]. For protons, the energy densities in central collisions may be large enough to create a quark-gluon-plasma, as well [44, 45]. Furthermore, microscopic effects in string fragmentation [46] and quantum chromodynamics interference [47] can also produce collective effects.

A decrease in the value of R in hadronic interactions in proton-proton collisions could

solve the muon puzzle [14]. However, collider data and hadronic interaction models constrain R: string fragmentation leads to $R \approx 0.4$, while statistical models suggest $R \approx 0.34$ [48]. In the core-corona approach [33], the dense interaction region behaves as a quark-gluon plasma and decays according to statistical hadronization (core). The remaining matter volume produces particles via string fragmentation (corona). As we will show in the present section, this behavior leads to a lower value of R.

4.1 Implementation in the CONEX framework

We implement a simplified version of the core-corona model [14] by changing the energy spectra of produced particles (see Sec. 2.1): the yield of the particle species i,

$$N_i = \omega_{\text{core}}\, N_i^{\text{core}} + (1 - \omega_{\text{core}})\, N_i^{\text{corona}},$$

has a contribution N_i^{core} from the statistical hadronization happening in the core and a contribution N_i^{corona} from the hadronization through string fragmentation in the corona region. We define ω_{core} as energy dependent (see equation 4.1 below).

In this approach, we only modify the hadronization, disregarding particle correlations from collective effects in the core, which we expect to be negligible. Collective effects can only influence the transversal momentum of particles, which is very low at high energies. We treat nuclei following the simplified superposition model. This simplification neglects nuclear effects, which would lead to a stronger core effect. Consequently, this simplification only implies a more conservative version of the core-corona approach. Furthermore, since core hadronization is experimentally demonstrated at mid-rapidity but not excluded for large rapidities, we uniformly apply the core-corona effect at all pseudorapidities, except for the leading particle, whose properties should not be modified. With the same argument, we apply the core-corona effect to all types of hadronic projectiles (nucleons, pions, and kaons). Finally, the core weight ω_{core} needs to increase monotonically with multiplicity to reflect collider data [48], starting from zero for low-multiplicity proton-proton scattering and reaching unity for central Pb-Pb collisions. Since in CONEX, the multiplicity of each hadronic interaction is not known event-by-event, but the mean multiplicity increases with the energy of the interaction [14], we can assume that the mean core fraction also increases monotonically with the energy:

$$\omega_{\text{core}}(E; E_{\text{acc}}, E_{\text{scale}}, f_\omega) = f_\omega \frac{\ln(E/E_{\text{acc}})}{\ln(E_{\text{scale}}/E_{\text{acc}})} \Theta(E - E_{\text{acc}}). \tag{4.1}$$

The Heaviside step function, Θ, ensures no core effects at energies below E_{acc}, where models are well constrained by accelerator data. We use a low threshold value of $E_{\text{acc}} = 100\,\text{GeV}$, since experimental data beyond fixed target measurements does not well constrain particle production in the relevant phase space. The parameter E_{scale} is a reference energy scale, where the modification scale f_ω is equal to the core fraction ω_{core}.

Since the energy spectra of secondary particles define the features of particle interactions, any modification to the energy spectra used in CONEX's cascade equations directly impacts the air shower simulation. We implement the core-corona approach by modifying these spectra, without changing the total amount of particles produced in the interactions. Each hadronic interaction model in CONEX has its own corona-type particle ratios for each energy bin, projectile, and secondary type. Referring to [49], we compute the respective core-type particle ratios using measurements of central Pb-Pb collisions, where we expect to have a 100% core effect. This way, we obtain the ratios $\pi^0/\pi^\pm$, $\text{p}/\pi^\pm$, $K^\pm/\pi^\pm$, p/n and $K^0/\pi^\pm$

that represent the core contribution. We directly obtain the charged pion, charged kaon, and proton yields using [49], and we add the decay products from the short-lived ϕ, Λ, Ξ and Ω particles [49] following the corresponding branching ratios. Finally, we deduce the neutral pion and neutron yields and compute the ratios using isospin invariance, given that the core- and corona-type ratios are independent of the interaction energy.

For each hadronic model, primary type and interaction energy, the total number of secondary particles at mid-rapidity is $N_{\rm tot} = N_{\pi^0} + N_{\pi^\pm} + N_{K^\pm} + N_{K^0} + N_{\rm p} + N_{\rm n}$, which needs to remain unchanged in the core-corona implementation. We can rewrite $N_{\rm tot} = A N_{\pi^\pm}$, where $A = 1 + R_{\pi^0/\pi^\pm} + R_{K^\pm/\pi^\pm} + R_{K^0/\pi^\pm} + R_{\rm p/\pi^\pm} + R_{\rm n/p} R_{\rm p/\pi^\pm}$, and $R_{\alpha/\beta} = N_\alpha / N_\beta$ is the ratio for particle species α and β. Suppose core-type hadronization produces all particles. In that case, the scale factors for the secondary particle spectra are $f_\alpha = \tilde{N}_\alpha / N_\alpha$, where N_α is the corona-type yield of the secondary particle type α and $\tilde{N}_\alpha$ is the corresponding yield from the core [49]. In an intermediate scenario, where $\omega_{\rm core}$ is between 0 and 1, the corresponding scale factor is $f_{\alpha,\omega} = 1 + (f_\alpha - 1)\ \omega_{\rm core}$. This way, we recover $f_{\alpha,\omega} = 1$ if $\omega_{\rm core} = 0$ and $f_{\alpha,\omega} = f_\alpha$ if $\omega_{\rm core} = 1$. To ensure that we preserve $N_{\rm tot}$ with the new particle ratios, we compute the new core-corona yields (denoted by the superscript $^{\rm cc}$) in the following order:

$$
\begin{aligned}
N^{\rm cc}_{\pi^\pm} &= N_{\rm tot} / A^{\rm cc} \\
N^{\rm cc}_{\pi^0} &= R^{\rm cc}_{\pi^0/\pi^\pm}\, N^{\rm cc}_{\pi^\pm} \\
N^{\rm cc}_{K^\pm} &= R^{\rm cc}_{K^\pm/\pi^\pm}\, N^{\rm cc}_{\pi^\pm} \\
N^{\rm cc}_{K^0} &= R^{\rm cc}_{K^0/\pi^0}\, N^{\rm cc}_{\pi^0} \\
N^{\rm cc}_{p} &= R^{\rm cc}_{p/\pi^\pm}\, N^{\rm cc}_{\pi^\pm} \\
N^{\rm cc}_{n} &= R^{\rm cc}_{n/\pi^0}\, N^{\rm cc}_{\pi^0}.
\end{aligned}
$$

For computing $N^{\rm cc}_{\pi^\pm}$, we need $N_{\rm tot}$ and $A^{\rm cc} = 1 + R^{\rm cc}_{\pi^0/\pi^\pm} + R^{\rm cc}_{K^\pm/\pi^\pm} + R^{\rm cc}_{K^0/\pi^\pm} + R^{\rm cc}_{\rm p/\pi^\pm} + R^{\rm cc}_{\rm n/p} R^{\rm cc}_{\rm p/\pi^\pm}$. We use the yields of the modified spectra to compute the new ratios.

Current hadronic interaction models implement different types of hadronization for the central part of the collision and the remnants [50]. String fragmentation describes the central part where most particles are produced at mid-rapidity, corresponding to a broad peak in the center of the energy spectra. The core-corona model applies to this region of interaction. Fig. 16 shows the neutral pion (left) and proton (right) energy spectra for three different proton-initiated shower energies with the default QGSJetII.04 hadronic interaction model (dashed black) and with an implementation of the core-corona model in QGSJetII.04 (solid red). The core-corona implementation leads to a decrease in the neutral pion spectra and an increase in the proton spectra.

The remnant hadronization mainly contributes when the secondary and projectile are the same particle type, giving rise to the *leading particle effect* (see Fig. 16, right). The corresponding spectrum has a *diffractive peak* at the projectile energy. Since the core-corona model does not affect the remnants, the diffractive peak must remain unaltered in the core-corona implementation. We modify the spectra with leading particle contribution conserving the total energy while leaving the diffractive peak untouched.

CONEX uses photon spectra derived from neutral pions in its electromagnetic cascade equations. Since the core-corona model modifies these neutral pion spectra, we must compute the new photon spectra. Considering that the decay $\pi^0 \to \gamma\gamma$ is isotropic in the rest frame, the distribution of produced photons is flat as a function of $\cos\theta^*$:

$$
\frac{{\rm d}N}{{\rm d}\cos\theta^*} = \frac{1}{2},
$$

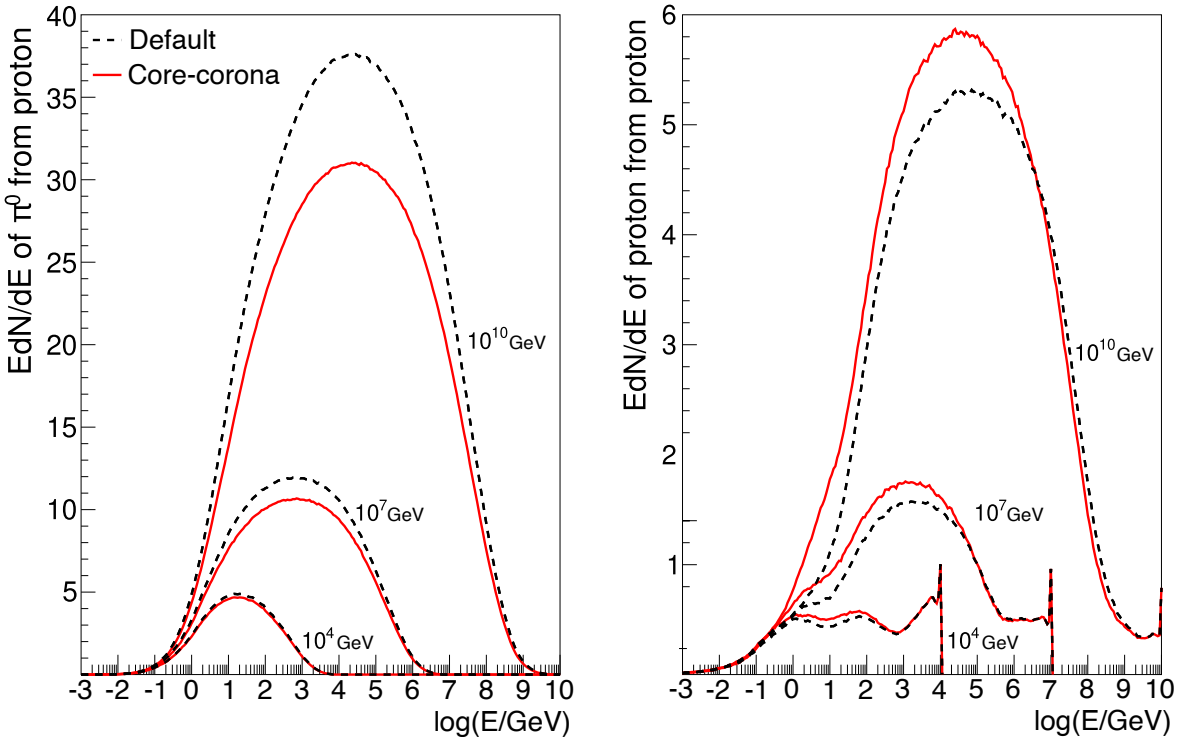

Figure 16: Default (dashed black) and modified (solid red) spectra of secondary particles for proton-air collisions at three different projectile energies using QGSJETII.04. Left: π^0, right: protons. The diffractive peak close to the projectile energy for proton secondaries reflects the leading particle effect.

where θ^* is the angle between the π^0 momentum in the laboratory frame and the photon momentum in the rest frame. We obtain the energy distribution of photons coming from a π^0 with momentum p_π from the transformation between rest and laboratory frames:

$$\frac{\mathrm{d}N}{\mathrm{d}E_\gamma} = \frac{1}{2}\frac{\mathrm{d}\cos\theta^*}{\mathrm{d}E_\gamma} = \frac{2}{p_\pi}.$$

We then calculate the number of photons with energy E_γ by integrating $2/p_\pi$ over all energies above E_γ. Finally, we apply a scale factor to the photons to ensure energy conservation after computing the new photon spectra based on the modified neutral pion spectra. We show the photon spectra obtained through this procedure, together with the original spectra, in Fig. 17. The differences between both at the highest energies produce a small change of $\pm 2\,\mathrm{g/cm^2}$ in $X_{\max}$, which can be corrected for each interaction model, if needed.

4.2 Air shower simulations

To assess the impact of the core-corona model on the muon-related observables, we focus on proton-initiated showers with $E_{\mathrm{scale}} = 10^{10}\,\mathrm{GeV}$ and $f_\omega = 1$. This leads to an ω_{core} value that increases logarithmically from 0 at $E = 10^2\,\mathrm{GeV}$ to a value of 1 at $E = 10^{10}\,\mathrm{GeV}$ (see Eq. 4.1). It is worth noting that the ω_{core} evolution with energy represents a rather strong contribution due to the core. However, it allows the production of muons in showers with a number compatible with observations [14].

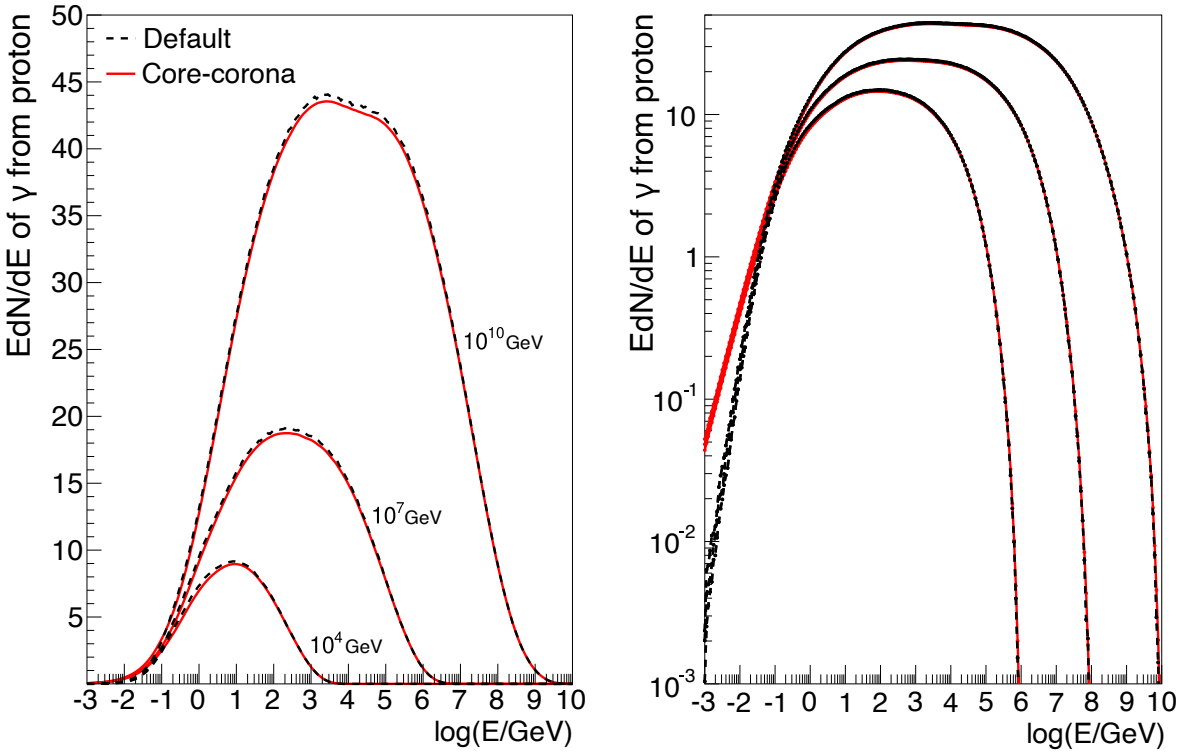

Figure 17: Energy spectra of photons arising from proton-air interactions with different energies using QGSJetII.04, with and without core-corona effect. Left: linear scale, right: logarithmic scale.

Figure 18 (left panel) shows the mean ratio of the muon number for a hadronic interaction model between the core-corona and default versions. We present results for EPOS LHC (black squares), QGSJetII.04 (red circles), and SIBYLL 2.3d (blue crosses) in the KASCADE, IceTop, and Auger scenarios. The core-corona model increases the muon number almost independently of the shower development stage (longitudinal profile), distance to the shower core, or energy of the muon at the ground. The ratio is highest at Auger (15% to 20%) and lowest at KASCADE (about 10%), which results from the primary cosmic ray energies considered in each case: the increase in the number of muons in the core-corona model scales with the primary particle energy. Finally, since QGSJetII.04 produces the lowest number of muons without modification, the impact of the core contribution is most significant. The evolution of the ratio with the incidence angle is rather flat in all experiments and hadronic interaction models. We display an example of the IceTop scenario in the right panel of Fig. 18.

This implementation of the core-corona model introduces only a global shift in the number of muons, since we only modify the particle ratios but not the spectral shape. The final number of muons depends on all the generations of the hadronic shower. In this approach, the modifications of hadronic interactions are significant only at high energy when no 3D development occurs. When the energy is low enough to allow for lateral spread, the hadronic interactions are not modified anymore. As a consequence, there is less energy going into the electromagnetic shower at high energy, allowing more muon production at low energy, but without a specific signature in the lateral distribution.

The effects of implementing the core-corona model at the Monte Carlo level would be

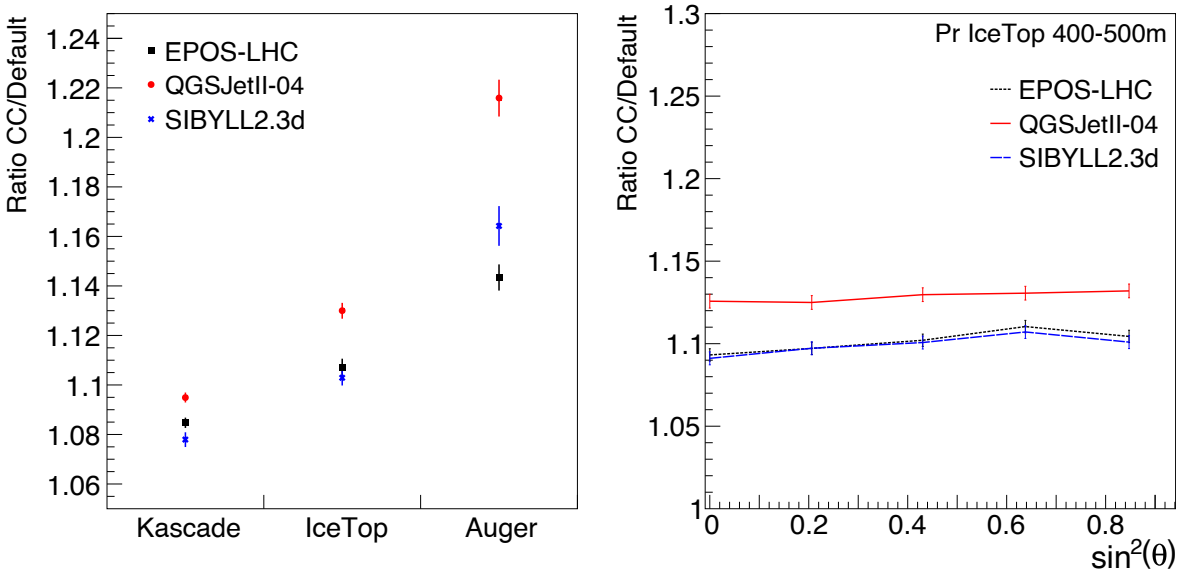

Figure 18: Mean ratio of the total numbers of muons in proton-initiated showers between the default hadronic interaction model and the corresponding core-corona implementation. Left: Vertical showers at different experiments, right: differently inclined showers at IceTop.

more intricate, as it can modify the transverse momentum of secondary particles. However, we anticipate minimal differences due to the forward boost, which mitigates the influence of these modifications. The primary particle type may have a larger impact, as heavier projectiles tend to produce a stronger core effect. Nevertheless, this would affect only the first interaction, limiting its overall impact. The core formation leads to a maximum increase of 15% to 20% in the number of muons under optimistic conditions. While this is a notable effect, it is insufficient to fully account for the Auger data unless $X_{\max}$ is also modified [51].

5 Conclusions

This paper presents advances in understanding the discrepancies between experimental data and theoretical models regarding the muon content in air showers.

We first addressed air shower simulations, an essential tool to interpret experimental data, by demonstrating that the CONEX framework significantly reduces computational costs compared to CORSIKA. Additionally, we introduced the CONEX 3D extension, which enables the study of lateral shower development—particularly the muon component—and showed that it reproduces full Monte Carlo simulations. This progress paves the way for performing more detailed simulations in low computing times.

Then, we applied the extended CONEX framework to study the interplay between various muon-related observables and the characteristics of three cosmic ray experiments sensitive to different shower characteristics: the Pierre Auger Observatory, the KASCADE Experiment, and the IceTop Array at IceCube. We examined how differences in muon observables—resulting from the geometry and sensitivities of each experiment—contribute to the model-data discrepancies. For this purpose, we analyzed the longitudinal and lateral distributions of muons, as well as the muon energy spectra. We also compared the cases of proton and iron-initiated showers.

Finally, leveraging the CONEX 3D fast and flexible structure, we presented the implementation of an effective core-corona model. This theory proposes that collective effects in proton-proton collisions significantly impact the hadronic shower content, partially explaining the muon deficit in air showers. We showed that underestimating the contribution of statistical hadronization in hadron-nuclei collisions may indeed lead to a muon deficit in simulations. In our implementation of the core-corona model, the core effect in hadronic interactions can be changed in an energy-dependent way. We showed that the muon ratio between the default hadronic interaction models and the corresponding core-corona implementation increases with the primary cosmic ray energy, similar to the discrepancy observed between air shower experiments and models. At a primary energy of $E_0 = 10^{19}\,\mathrm{eV}$, we obtained an increase of 15% to 20% in the muon content, considering a high contribution due to the core. Consequently, to explain the muon deficit observed with the current hadronic interaction models, various models could be considered. But since the effect of collective hadronization was observed at the LHC, including the core-corona model in hadronic interactions is necessary before considering more exotic scenarios.

Acknowledgments

The authors would like to thank Nikolai Kalmikov, Vladimir Chernatkin and Klaus Werner for the fruitful discussions and their initial work on the electromagnetic cascade equations and Sergey Ostapchenko for his first work on the muon 3D propagation in CONEX.

References

1. Engel, R., Heck, D. & Pierog, T. Extensive air showers and hadronic interactions at high energy. *Annual review of nuclear and particle science* **61,** 467–489 (2011).
2. Matthews, J. A Heitler model of extensive air showers. *Astroparticle Physics* **22,** 387–397 (2005).
3. Kampert, K.-H. & Unger, M. Measurements of the cosmic ray composition with air shower experiments. *Astroparticle Physics* **35,** 660–678 (2012).
4. Albrecht, J. *et al.* The Muon Puzzle in cosmic-ray induced air showers and its connection to the Large Hadron Collider. *Astrophysics and Space Science* **367,** 27 (2022).
5. Cazon, L. Working group report on the combined analysis of muon density measurements from eight air shower experiments. *arXiv preprint arXiv:2001.07508* (2020).
6. Meurer, C., Blümer, J., Engel, R., Haungs, A. & Roth, M. Muon production in extensive air showers and its relation to hadronic interactions. *Czechoslovak Journal of Physics* **56,** A211–A219 (2006).
7. Aab, A. *et al.* The pierre auger observatory upgrade-preliminary design report. *arXiv preprint arXiv:1604.03637* (2016).
8. Abbasi, R. *et al.* IceTop: The surface component of IceCube. *Nuclear Instruments and Methods in Physics Research Section A: Accelerators, Spectrometers, Detectors and Associated Equipment* **700,** 188–220 (2013).
9. Apel, e. W. *et al.* The KASCADE-grande experiment. *Nuclear Instruments and Methods in Physics Research Section A: accelerators, spectrometers, detectors and associated equipment* **620,** 202–216 (2010).

10. Collaboration, P. A. *et al.* The Pierre auger observatory and its upgrade. *Science Reviews-from the end of the world* **1,** 8–33 (2020).

11. Ranchon, S. & Urban, M. Response of a Pierre Auger Observatory surface detector to MeV electrons and GeV muons. *Nuclear Instruments and Methods in Physics Research Section A: Accelerators, Spectrometers, Detectors and Associated Equipment* **538,** 483–495 (2005).

12. Aab, A. *et al.* Design, upgrade and characterization of the silicon photomultiplier front-end for the AMIGA detector at the Pierre Auger Observatory. *Journal of Instrumentation* **16,** P01026 (2021).

13. Antoni, e. T. *et al.* The cosmic-ray experiment KASCADE. *Nuclear Instruments and Methods in Physics Research Section A: accelerators, spectrometers, detectors and associated equipment* **513,** 490–510 (2003).

14. Baur, S. *et al.* Core-corona effect in hadron collisions and muon production in air showers. *Physical Review D* **107,** 094031 (2023).

15. Heck, D., Knapp, J., Capdevielle, J., Schatz, G., Thouw, T., *et al.* CORSIKA: A Monte Carlo code to simulate extensive air showers. *Report fzka* **6019** (1998).

16. Bergmann, T. *et al.* One-dimensional hybrid approach to extensive air shower simulation. *Astroparticle Physics* **26,** 420–432 (2007).

17. Dedenko, L. *A new method of solving the nuclear cascade equation.* in *International Cosmic Ray Conference* **2** (1965), 662.

18. Hillas, A. *Calculations on the propagation of mesons in extensive air showers* in *International Cosmic Ray Conference* **2** (1965), 758.

19. Stanev, T. & Vankov, H. P. Hybrid simulations of electromagnetic cascades. *Astropart. Phys.* **2,** 35–42 (1994).

20. Drescher, H.-J. & Farrar, G. R. Air shower simulations in a hybrid approach using cascade equations. *Phys. Rev. D* **67,** 116001. arXiv: astro-ph/0212018 (2003).

21. Bossard, G. *et al.* Cosmic ray air shower characteristics in the framework of the parton-based Gribov-Regge model NEXUS. *Physical Review D* **63,** 054030 (2001).

22. Pierog, T., Karpenko, I., Katzy, J. M., Yatsenko, E. & Werner, K. EPOS LHC: Test of collective hadronization with data measured at the CERN Large Hadron Collider. *Phys. Rev. C* **92,** 034906. arXiv: 1306.0121 [hep-ph] (2015).

23. Ostapchenko, S. Monte Carlo treatment of hadronic interactions in enhanced Pomeron scheme: I. QGSJET-II model. *Phys. Rev. D* **83,** 014018. arXiv: 1010.1869 [hep-ph] (2011).

24. Riehn, F., Engel, R., Fedynitch, A., Gaisser, T. K. & Stanev, T. Hadronic interaction model Sibyll 2.3d and extensive air showers. *Phys. Rev. D* **102,** 063002. arXiv: 1912.03300 [hep-ph] (2020).

25. Pierog, T., Engel, R., Heck, D. & Ulrich, R. *3D Hybrid Air Shower Simulation in CORSIKA* in *32nd International Cosmic Ray Conference* **2** (2011), 222.

26. Chernatkin, V., Kalmykov, N. & Werner, K. Three dimensional electron photon cascade. *Surveys High Energ. Phys.* **18** (eds Kaidalov, A. B. & Vysotsky, M. I.) 183–186 (2003).

27. Chernatkin, V. *Simulation des gerbes dues aux rayons cosmiques a très hautes énergies* PhD thesis (Université de Nantes, 2005).

28. Heck, D. & Pierog, T. Extensive Air Shower Simulation with CORSIKA: A User's Guide (Version 7.7550 from April 30, 2024).

29. Müller, S. *Direct measurement of the muon density in air showers with the Pierre Auger Observatory* in *EPJ Web of Conferences* **210** (2019), 02013.

30. Manshanden, J., Sigl, G. & Garzelli, M. V. Modeling strangeness enhancements to resolve the muon excess in cosmic ray extensive air shower data. *JCAP* **02,** 017. arXiv: 2208.04266 [hep-ph] (2023).

31. Werner, K., Pierog, T., Guiot, B. & Jahan, J. Recent Developments in EPOS: Core–Corona Effects in Air Showers? *Phys. At. Nucl.* **84,** 1026–1029 (2021).

32. Anchordoqui, L. A., Canal, C. G., Kling, F., Sciutto, S. J. & Soriano, J. F. An explanation of the muon puzzle of ultrahigh-energy cosmic rays and the role of the Forward Physics Facility for model improvement. *JHEAp* **34,** 19–32. arXiv: 2202.03095 [hep-ph] (2022).

33. Werner, K. Core-corona separation in ultrarelativistic heavy ion collisions. *Physical review letters* **98,** 152301 (2007).

34. Adams, J. *et al.* Experimental and theoretical challenges in the search for the quark gluon plasma: The STAR Collaboration's critical assessment of the evidence from RHIC collisions. *Nuclear Physics A* **757,** 102–183 (2005).

35. Adcox, K. *et al.* Formation of dense partonic matter in relativistic nucleus–nucleus collisions at RHIC: experimental evaluation by the PHENIX collaboration. *Nuclear Physics A* **757,** 184–283 (2005).

36. Arsene, I. *et al.* Quark gluon plasma and color glass condensate at RHIC? The perspective from the BRAHMS experiment. *Nuclear Physics A* **757,** 1–27 (2005).

37. Back, B. *et al.* The PHOBOS perspective on discoveries at RHIC. *Nuclear Physics A* **757,** 28–101 (2005).

38. Chatrchyan, S. *et al.* Observation of long-range, near-side angular correlations in proton–lead collisions at the LHC. *Physics Letters B* **718,** 795–814 (2013).

39. Dusling, K., Li, W. & Schenke, B. Novel collective phenomena in high-energy proton–proton and proton–nucleus collisions. *International Journal of Modern Physics E* **25,** 1630002 (2016).

40. Loizides, C. Experimental overview on small collision systems at the LHC. *Nuclear Physics A* **956,** 200–207 (2016).

41. Shuryak, E. V. Quantum chromodynamics and the theory of superdense matter. *Physics Reports* **61,** 71–158 (1980).

42. Stoecker, H. & Greiner, W. High energy heavy ion collisions—probing the equation of state of highly excited hardronic matter. *Physics Reports* **137,** 277–392 (1986).

43. Kolb, P. F. & Heinz, U. Hydrodynamic description of ultrarelativistic heavy-ion collisions. *Quark–Gluon Plasma 3,* 634–714 (2004).

44. Werner, K., Karpenko, I. & Pierog, T. The "Ridge" in Proton-Proton Scattering at 7 TeV. *Physical Review Letters* **106,** 122004 (2011).

45. Nagle, J. L. & Zajc, W. A. Small system collectivity in relativistic hadronic and nuclear collisions. *Annual Review of Nuclear and Particle Science* **68,** 211–235 (2018).

46. Bierlich, C., Gustafson, G. & Lönnblad, L. Collectivity without plasma in hadronic collisions. *Physics Letters B* **779,** 58–63 (2018).

47. Blok, B., Jäkel, C. D., Strikman, M. & Wiedemann, U. A. Collectivity from interference. *Journal of High Energy Physics* **2017,** 1–50 (2017).

48. Enhanced production of multi-strange hadrons in high-multiplicity proton–proton collisions. *Nature Physics* **13,** 535–539 (2017).

49. Andronic, A., Braun-Munzinger, P., Redlich, K. & Stachel, J. *Hadron yields, the chemical freeze-out and the QCD phase diagram* in *Journal of Physics: Conference Series* **779** (2017), 012012.

50. Ayala, A. *et al.* Core meets corona: A two-component source to explain Λ and Λ global polarization in semi-central heavy-ion collisions. *Physics Letters B* **810,** 135818 (2020).

51. Abdul Halim, A. *et al.* Testing hadronic-model predictions of depth of maximum of air-shower profiles and ground-particle signals using hybrid data of the Pierre Auger Observatory. *Physical Review D* **109,** 102001 (2024).